

## ALMA OBSERVATIONS OF A GAP AND A RING IN THE PROTOPLANETARY DISK AROUND TW HYA

HIDEKO NOMURA<sup>1,\*</sup>, TAKASHI TSUKAGOSHI<sup>2,\*</sup>, RYOHEI KAWABE<sup>3,4,5</sup>, DAIKI ISHIMOTO<sup>6,1</sup>, SATOSHI OKUZUMI<sup>1</sup>, TAKAYUKI MUTO<sup>7</sup>, KAZUHIRO D. KANAGAWA<sup>8</sup>, SHIGERU IDA<sup>9</sup>, CATHERINE WALSH<sup>10</sup>, T.J. MILLAR<sup>11</sup> AND XUE-NING BAI<sup>12</sup>*Draft version February 29, 2016*

## ABSTRACT

We report the first detection of a gap and a ring in 336GHz dust continuum emission from the protoplanetary disk around TW Hya, using the Atacama Large Millimeter/Submillimeter Array (ALMA). The gap and ring are located at around 25 and 41 AU from the central star, respectively, and are associated with the CO snow line at  $\sim 30$  AU. The gap has a radial width of less than 15 AU and a mass deficit of more than 23%, taking into account that the observations are limited to an angular resolution of  $\sim 15$  AU. In addition, the  $^{13}\text{CO}$  and  $\text{C}^{18}\text{O}$   $J = 3 - 2$  lines show a decrement in CO line emission throughout the disk, down to  $\sim 10$  AU, indicating a freeze-out of gas-phase CO onto grain surfaces and possible subsequent surface reactions to form larger molecules. The observed gap could be caused by gravitational interaction between the disk gas and a planet with a mass less than super-Neptune ( $2M_{\text{Neptune}}$ ), or could be the result of the destruction of large dust aggregates due to the sintering of CO ice.

*Subject headings:* protoplanetary disks — stars: individual (TW Hya) — submillimeter: planetary systems — planet-disk interactions — molecular processes

## 1. INTRODUCTION

The physical structures and chemical compositions of gas, dust, and ice in protoplanetary disks control the formation process of planets and the composition of their cores and atmospheres. The ALMA long baseline campaign has detected gaps and rings in dust continuum emission from the circumstellar disk around a very young star ( $\sim 0.1 - 1$  Myrs), HL Tau (ALMA Partnership et al. 2015). The origin of this complex disk structure in such a young object remains under debate.

In this Letter, we present ALMA observations of the relatively old ( $\sim 3 - 10$  Myrs) gas-rich disk around the young Sun-like star, TW Hya ( $\sim 0.8M_{\odot}$ ), which show

the presence of a gap and a ring associated with the CO snow line. TW Hya's proximity ( $54 \pm 6$  pc) makes it an ideal source to study formation environment of a planetary system (e.g., Andrews et al. 2012). The disk is old compared with other gas-rich protoplanetary disks whose lifetime is typically  $\sim 3$  Myrs (e.g., Hernández et al. 2007). Nevertheless, the disk gas mass is  $> 0.05M_{\odot}$  inferred through HD line observations with *Herschel* (Bergin et al. 2013). In exoplanetary systems giant planets have been discovered at/beyond Neptune-orbit around Sun-like stars by direct imaging observations using Subaru/HiCIAO (Thalmann et al. 2009; Kuzuhara et al. 2013). Thus, planets are able to form even at large distances within disk lifetime by, for example, scattering of planetary cores (Kikuchi et al. 2014). Given that planet-disk interaction is key for planet orbital evolution and planet population synthesis (e.g., Kley & Nelson 2012; Ida et al. 2013), understanding gap formation in protoplanetary disks helps to gain insight into the early evolution of our own Solar System, as well as the observed diversity of exoplanetary systems.

## 2. OBSERVATIONS AND DATA REDUCTION

TW Hya was observed with ALMA in Band 7 on 20-21 May, 2015 with 40 antennas in Cycle 2 with a uv-coverage of 22-580 k $\lambda$  (PI: D. Ishimoto). The spectral windows were centered at 329.295GHz (SPW1), 330.552GHz (SPW0), 340.211GHz (SPW2), and 342.846GHz (SPW3), covering  $\text{C}^{18}\text{O}$   $J = 3 - 2$ ,  $^{13}\text{CO}$   $J = 3 - 2$ ,  $\text{CN}$   $N = 3 - 2$  and  $\text{CS}$   $J = 7 - 6$ . The channel spacing was  $\delta\nu = 30.52\text{kHz}$  and the bandwidth was 117.188MHz except for SPW 2 in which a channel spacing of  $\delta\nu = 15.26\text{kHz}$  and a bandwidth of 58.594MHz were used. The quasar J1058+0133 was observed as a bandpass calibrator while the nearby quasar J1037-2934 was used for phase and gain calibration. The mean flux density of J1037-2934 was 0.58Jy during the observation period.

The visibility data were reduced and calibrated using

nomura@geo.titech.ac.jp

<sup>1</sup> Department of Earth and Planetary Sciences, Tokyo Institute of Technology, 2-12-1 Ookayama, Meguro, Tokyo, 152-8551, Japan<sup>2</sup> College of Science, Ibaraki University, Mito, Ibaraki 310-8512, Japan<sup>3</sup> National Astronomical Observatory of Japan, 2-21-1 Osawa, Mitaka, Tokyo 181-8588, Japan<sup>4</sup> SOKENDAI (The Graduate University for Advanced Studies), 2-21-1 Osawa, Mitaka, Tokyo 181-8588, Japan<sup>5</sup> Department of Astronomy, School of Science, University of Tokyo, Bunkyo, Tokyo 113-0033, Japan<sup>6</sup> Department of Astronomy, Graduate School of Science, Kyoto University, Kitashirakawa-Oiwake-cho, Sakyo-ku, Kyoto 606-8502, Japan<sup>7</sup> Division of Liberal Arts, Kogakuin University, 1-24-2 Nishi-Shinjuku, Shinjuku-ku, Tokyo, 163-8677, Japan<sup>8</sup> Institute of Low Temperature Science, Hokkaido University, Sapporo 060-0819, Japan<sup>9</sup> Earth-Life Science Institute, Tokyo Institute of Technology, 2-12-1 Ookayama, Meguro, Tokyo 152-8550, Japan<sup>10</sup> Leiden Observatory, Leiden University, P. O. Box 9513, 2300 RA Leiden, The Netherlands<sup>11</sup> Astrophysics Research Centre, School of Mathematics and Physics, Queen's University Belfast, University Road, Belfast BT7 1NN, UK<sup>12</sup> Institute for Theory and Computation, Harvard-Smithsonian Center for Astrophysics, 60 Garden Street, MS-51, Cambridge, MA 02138, USA

\* These authors contributed equally to this work.

CASA, version 4.3.1 and 4.4.0. The visibility data was reduced for each SPW separately, and the continuum visibilities were extracted by averaging the line-free channels in all SPWs. The corrected visibilities were imaged using the CLEAN algorithm with Briggs weighting with a robust parameter of 0 after calibration of the bandpass, gain in amplitude and phase, and absolute flux scaling, and then flagging for aberrant data. In addition to the usual CLEAN imaging, we performed self-calibration of the continuum emission to improve the sensitivity and image quality. The obtained solution table of the self-calibration for the continuum emission was applied to the visibilities of the lines. The self-calibration significantly improved the sensitivity of the continuum image by one order of magnitude from 2.6 to 0.23 mJy. In addition, the continuum visibility data with deprojected baselines longer than 200 k $\lambda$  was extracted in order to enhance small scale structure around the gap. The high spatial resolution data was analysed in a similar way, but imaged using the CLEAN algorithm with uniform weighting. Also, the ALMA archived data of N<sub>2</sub>H<sup>+</sup>  $J = 4 - 3$  line at 372.672 GHz were reanalysed in a similar way to compare with that obtained by our observations. The re-analysed data is consistent with that in Qi et al. (2013). For the N<sub>2</sub>H<sup>+</sup> line data, the synthesized beam and the 1 $\sigma$  RMS noise level in 0.1 km s<sup>-1</sup> were 0."44 $\times$ 0."41 ( $P.A. = 12.4^\circ$ ) and 31.2 mJy beam<sup>-1</sup>.

### 3. RESULTS

#### 3.1. Dust Continuum Emission

The observed dust continuum emission maps at 336 GHz are plotted for both the full data (Fig. 1a) and high spatial frequencies only ( $> 200$  k $\lambda$ , Fig. 1b). The synthesized beam and RMS noise were 0."37 $\times$ 0."31 ( $\sim 20$  AU,  $P.A. = 55.7^\circ$ ) and 0.23 mJy beam<sup>-1</sup>. The total and peak flux density were 1.41 Jy and 0.15 Jy beam<sup>-1</sup> with a SN (signal-to-noise) ratio of 705 and 652, respectively. The results agree well with the previous SMA observations (Andrews et al. 2012) and ALMA observations (Hogerheijde et al. 2015) with lower spatial resolution and sensitivity. The synthesized beam and RMS for the data at high spatial resolution data only were 0."32 $\times$ 0."26 ( $\sim 15$  AU,  $P.A. = 54.5^\circ$ ) and 0.49 mJy beam<sup>-1</sup>.

As shown by the black line in Fig. 2a, the dust continuum emission of the full data has a shallow dip in the radial profile of the surface brightness obtained by deprojecting the observed image data assuming an inclination angle of  $7^\circ$  and a position angle of  $-30^\circ$  (Qi et al. 2008). By imaging the data at high spatial frequencies only ( $> 200$  k $\lambda$ ), we identify a gap and a ring at around 25 AU and 41 AU, respectively (Fig. 1b and gray line in Fig. 2a). The uv-coverage of the full data set (from 22 to 580 k $\lambda$ ) is sufficiently high and indeed vital for this analysis. The continuum visibility profile as a function of the deprojected baseline length is plotted in Fig. 3. Our result is consistent with the recent ALMA observations with higher spatial resolution and sensitivity (Zhang et al. 2016). Since the high spatial frequency data misses flux of spatially extended structure, the total flux is lower than that of the full data by an order of magnitude. Artificial structure appears at  $R > 70$  AU in the high spatial frequency data probably due to a fail-

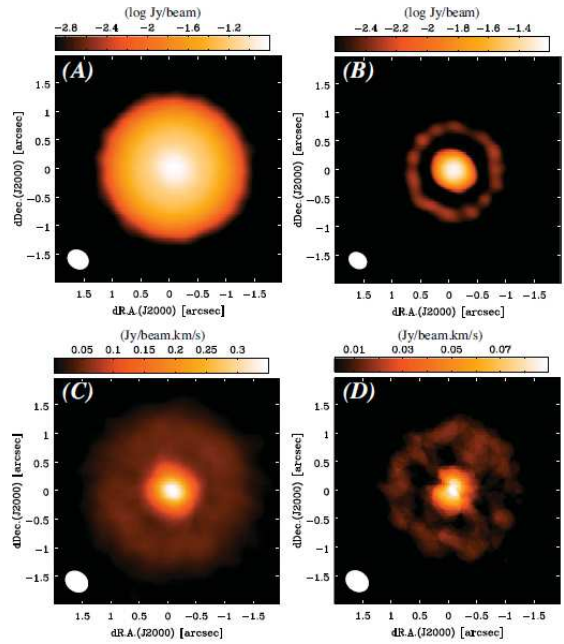


FIG. 1.— 336 GHz dust continuum map imaged using (A) all spatial frequency data and (B) only high spatial frequency ( $> 200$  k $\lambda$ ) data, (C)  $^{13}\text{CO}$   $J = 3 - 2$  and (D)  $\text{C}^{18}\text{O}$   $J = 3 - 2$  integrated line emission maps. Emission less than  $5\sigma$ -noise-level were masked. The synthesized beam sizes are shown in the bottom left corner of each panel.

ure to subtract the side lobe pattern of the synthesized beam. Its intensity is less than the  $2\sigma$ -noise-level and the structure is masked in Fig. 2a. The location of the gap is similar to that of the axisymmetric depression in polarized intensity of near-infrared scattered light imaging of dust grains recently found by Subaru/HiCIAO and Gemini/GPI (Akiyama et al. 2015; Rapson et al. 2016).

#### 3.2. Dust Surface Density and Gap Parameters

We extract the radial dust surface density distribution (Fig. 2b), using the deprojected data of the dust continuum emission and the equation,

$$I_{d,\nu} = B_\nu(T_d)[1 - \exp(-\tau_{d,\nu})], \quad (1)$$

where  $I_{d,\nu}$  is the observed intensity of the dust continuum emission at the frequency  $\nu$ ,  $B_\nu(T_d)$  is the Planck function at the dust temperature,  $T_d$ . The optical depth,  $\tau_{d,\nu}$ , is defined as  $\tau_{d,\nu} = \kappa_\nu \Sigma_{\text{dust}}$ , where  $\Sigma_{\text{dust}}$  is the dust surface density and the dust opacity,  $\kappa_\nu$ , is set as  $\kappa_\nu = 3.4 \text{ cm}^2 \text{ g}^{-1}$ . We adopt  $T_d = 22 \text{ K} (R/10 \text{ AU})^{-0.3}$ , where  $R$  is the disk radius, by fitting the model result in Andrews et al. (2012) and assume a uniform temperature distribution in the vertical direction. The derived dust surface density is shown in Fig. 2c. We note that the derived dust surface density distribution is consistent with that derived from SMA observations of dust continuum emission and model calculations (Andrews et al. 2012). Also, the assumed dust temperature is consistent with the color temperature obtained from the spectral index of continuum emission across the observed four basebands between 329 GHz and 343 GHz (Fig. 2d) in the optically thick regions ( $\leq 30$  AU, Fig. 2c).

To estimate the gap width,  $\Delta_{\text{gap}}$ , and depth,  $(\Sigma_0 - \Sigma)/\Sigma_0$ , where  $\Sigma_0$  and  $\Sigma$  are the basic surface density and the surface density with the gap at the gap center,

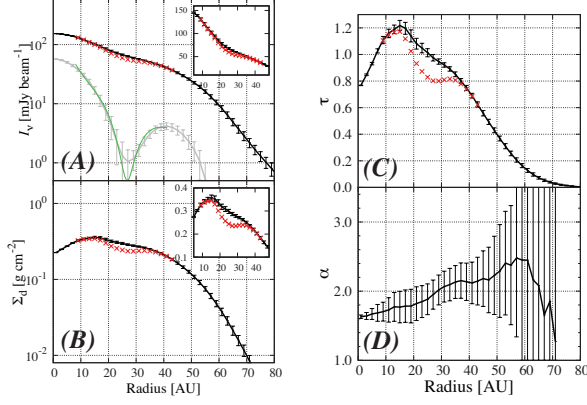


FIG. 2.— Radial distributions of (A) intensity of 336GHz dust continuum emission, (B) dust surface density, (C) optical depth and (D) spectral index between 329GHz and 343GHz. Gray line in Figure (A) shows the data of only high spatial frequency with its Gaussian fit (green line). Red crosses in (A)-(C) are derived from high spatial frequency data recovered by the full spatial frequency data at the gap. The inserts show a close-up of the region around the gap.

the intensity at the gap,  $I_{\text{gap}}$  (red crosses in Fig. 2a), is derived by completing the missing flux of the high spatial frequency data,  $I_{\text{gap}}^{\text{high}}$  (gray line in Fig. 2a), with the full spatial frequency data,  $I^{\text{full}}$  (black line in Fig. 2a). The intensity profile across the gap was obtained as follows; (i) fit the high frequency data without the gap using a power-law profile of  $I_0^{\text{high}} = 1.1 \times 10^3 R_{\text{AU}}^{-1.5}$  mJy beam $^{-1}$ , (ii) fit the gap region in the high frequency data using a single Gaussian profile of  $\Delta I_{\text{gap}} = I_0^{\text{high}} - I_{\text{gap}}^{\text{high}} = 7.7 \exp(-(R_{\text{AU}} - 24.7 \text{AU})^2 / \{2(5.9 \text{AU})^2\})$  mJy beam $^{-1}$  (whose FWHM is  $13.9 \pm 1.0 \text{AU}$  and depth is  $7.7 \pm 0.5 \text{mJy}$ ) (green line in Fig. 2a) and (iii) obtain the intensity at the gap as  $I_{\text{gap}} = I^{\text{full}} - \Delta I_{\text{gap}}$ , where  $I^{\text{full}}$  is the intensity of the full data. In this fitting, we adopted the edges of the gap at  $R = 9 - 13 \text{AU}$  (inner edge) and  $39 - 43 \text{AU}$  (outer edge) so that  $\Delta I_{\text{gap}}$  is overlaid to  $I^{\text{full}}$  smoothly. The optical depth at the gap is derived using  $I_{\text{gap}}$  and Eq.(1), and then the dust surface density at the gap is derived using the same method mentioned above (red crosses in Fig. 2b). The resulting gap width is  $\Delta_{\text{gap}} \sim 15 \text{AU}$  and the depth is  $(\Sigma_0 - \Sigma) / \Sigma_0 \sim 0.23$ . We note that our estimate of the gap width is limited by the angular resolution of the high spatial frequency data. The pattern of the gap and ring is also affected by residual artefacts due to the cut-off at  $200 \text{k}\lambda$ , which introduces uncertainties in the location of the gap center, and the width and depth of the gap.

### 3.3. CO Isotopologue Line Emission

The observed  $^{13}\text{CO}$  and  $\text{C}^{18}\text{O}$   $J = 3 - 2$  rotational line emission maps are plotted in Figs. 1c and 1d. The resulting synthesized beam and the  $1\sigma$  RMS noise level in  $0.03 \text{ km s}^{-1}$  width-channels were  $0.''41 \times 0.''33$  ( $P.A. = 53.4^\circ$ ),  $12.0 \text{mJy beam}^{-1}$  ( $^{13}\text{CO}$ ) and  $0.''41 \times 0.''33$  ( $P.A. = 53.8^\circ$ ),  $13.4 \text{mJy beam}^{-1}$  ( $\text{C}^{18}\text{O}$ ). The integrated intensity maps were created by integrating from  $1.18$  to  $4.30 \text{ km s}^{-1}$  ( $^{13}\text{CO}$ ) and from  $1.48$  to  $4.15 \text{ km s}^{-1}$  ( $\text{C}^{18}\text{O}$ ). The resultant noise levels of the map were  $8.4 \text{ mJy beam}^{-1} \text{ km s}^{-1}$  ( $^{13}\text{CO}$ ) and  $6.5 \text{ mJy beam}^{-1} \text{ km s}^{-1}$  ( $\text{C}^{18}\text{O}$ ). The deprojected radial profiles of the integrated line emission of the  $^{13}\text{CO}$  and  $\text{C}^{18}\text{O}$  following subtraction of the dust

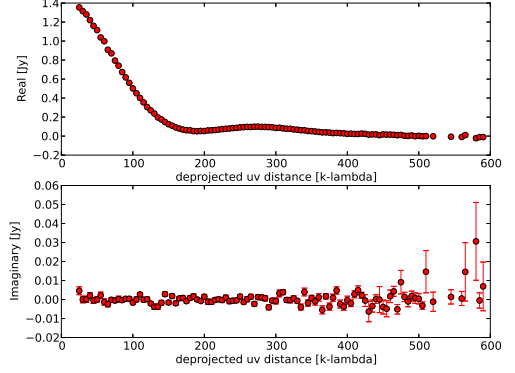


FIG. 3.— Real (top) and imaginary (bottom) parts of the azimuthally averaged continuum visibility profile as a function of the deprojected baseline length.

continuum emission are plotted in Fig. 4a. The signal-to-noise ratio is not sufficiently high to analyse the high spatial resolution data only.

### 3.4. CO Column Density

We obtain the CO radial column density distribution, using the deprojected data of the  $^{13}\text{CO}$  and  $\text{C}^{18}\text{O}$  line observations (Fig. 4d). The CO column density,  $N_{\text{CO}}$ , is derived from the integrated line emission of the  $\text{C}^{18}\text{O}$   $J = 3 - 2$  (Turner 1991; Rybicki & Lightman 1979), assuming the abundance ratios of  $\text{CO} : ^{13}\text{CO} = 67 : 1$  and  $^{13}\text{CO} : \text{C}^{18}\text{O} = 7 : 1$  (Qi et al. 2011). The optical depth of the  $\text{C}^{18}\text{O}$  line emission,  $\tau_{\text{C}^{18}\text{O},v}$  (Fig. 4c), is obtained from the observed line intensity as follows. We assume that the CO line emitting region is mainly in the surface layer, while the dust continuum emitting region is near the midplane. Thus, the deprojected intensity of the CO line emission plus dust continuum emission can be approximately derived from the following equation by simply assuming three zones in the vertical direction of the disk,

$$I_{\text{C}^{18}\text{O}+\text{cont},v} = B_\nu(T_g)(1 - e^{-\tau_{\text{C}^{18}\text{O},v}/2}) + B_\nu(T_d)(1 - e^{-\tau_{d,v}})e^{-\tau_{\text{C}^{18}\text{O},v}/2} + B_\nu(T_g)(1 - e^{-\tau_{\text{C}^{18}\text{O},v}/2})e^{-\tau_{d,v}-\tau_{\text{C}^{18}\text{O},v}/2}, \quad (2)$$

where  $T_g$  is the gas temperature of the CO line emitting region and  $T_d$  is the dust temperature near the midplane. The data continuum-subtracted data,  $I_{\text{C}^{18}\text{O}+\text{cont},v} - I_{d,v}$ , together with Eq.(1) is used for the analysis. Since the observed line ratio of  $\int I_{\text{C}^{18}\text{O},v} dv / \int I_{^{13}\text{CO},v} dv$  is larger than  $1/7$  (Fig. 4b), the  $^{13}\text{CO}$  line is optically thick. Therefore, we adopt the brightness temperature at the peak of the  $^{13}\text{CO}$  line (Fig. 5) as the gas temperature,  $T_g$ . Also, we adopt a dust temperature of  $T_d = 22 \text{K} (R/10 \text{AU})^{-0.3}$  and the dust optical depth,  $\tau_{d,v}$ , is derived from the dust continuum observations (Fig. 2c). We note that in the analysis we simply assume that the gas temperature is uniform in the vertical direction, and the gas temperature of the  $\text{C}^{18}\text{O}$  line emitting region is the same as that of the  $^{13}\text{CO}$  line emitting region, although it could be lower in reality. In addition,  $\text{C}^{18}\text{O}$  could be depleted due to the effect of isotopologue-dependent photodissociation, and  $N_{\text{CO}}/N_{\text{C}^{18}\text{O}}$  is possi-



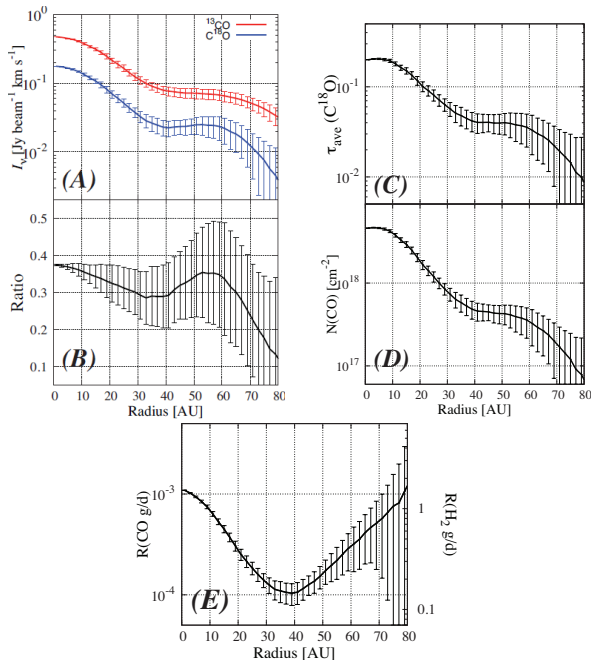


FIG. 4.— Radial distributions of (A) integrated line emission of  $^{13}\text{CO}$  (red line) and  $\text{C}^{18}\text{O}$  (blue line)  $J = 3 - 2$ , (B) line ratio of  $\text{C}^{18}\text{O}$  to  $^{13}\text{CO}$ , (C) averaged optical depth of the  $\text{C}^{18}\text{O}$  line, (D) CO column density and (E) CO gas-to-dust surface density ratio.  $\text{H}_2$  gas-to-dust ratio is also marked for a reference by simply assuming the abundance ratio of CO to  $\text{H}_2$  of  $6 \times 10^{-5}$ . All data are smoothed to a beam size of  $0.''45 \times 0.''45$ .

bly higher than 440 (Miotello et al. 2014). The CO column density will be underestimated due to these effects.

### 3.5. CO Gas-to-Dust Surface Density Ratio

Using the obtained CO column density and dust surface density (Figs. 4d and 2b), we derive the CO gas-to-dust surface density ratio (Fig. 4e). If we convert it to the  $\text{H}_2$  surface density, assuming an abundance ratio of CO to  $\text{H}_2$  of  $6 \times 10^{-5}$  (Qi et al. 2011), the estimated  $\text{H}_2$  gas mass is orders of magnitude lower than that predicted from the observations of the HD line emission by the Herschel Space Observatory (Bergin et al. 2013). The resulting  $\text{H}_2$  gas-to-dust surface density ratio ( $\sim 0.1 - 1$ ) is about two orders of magnitude lower than the typical interstellar value of  $\sim 100$ , which suggests strong CO depletion throughout the disk down to  $\sim 10\text{AU}$ .

The CO gas-to-dust surface density ratio increases beyond a radius of  $\sim 40\text{AU}$  since the dust surface density drops dramatically in this region. It could be due to drift of pebbles from the outer disk toward the central star (e.g. Takeuchi et al. 2005; Andrews et al. 2012; Walsh et al. 2014b).

## 4. DISCUSSIONS

### 4.1. Origin of the Gap and Ring in the Dust Continuum Emission

The gap and ring resemble those in the HL Tau system, recently found by the ALMA long baseline campaign (ALMA Partnership et al. 2015). Our result shows that gaps and rings in the (sub)millimeter dust continuum can exist, not only in relatively young disks ( $0.1 - 1\text{Myrs}$ ) but also in relatively old disks ( $3 - 10\text{Myrs}$ ). One possible mechanism to open a gap is

the gravitational interaction between a planet and the gas (e.g., Lin & Papaloizou 1979; Goldreich & Tremaine 1980; Fung et al. 2014). Such an interaction may also produce the spiral density waves recently found in optical and near-infrared scattered light imaging of dust grains in protoplanetary disks (e.g., Muto et al. 2012). According to recent theoretical analyses of gap structure around a planet (Kanagawa et al. 2015a,b, 2016), the depth and width of the gap are controlled by the planetary mass, the turbulent viscosity and the gas temperature. The shape of the gap is strongly influenced by angular momentum transfer via turbulent viscosity and/or instability caused by a steep pressure gradient at the edges of a gap. The observed gap has an apparent width and depth of  $\Delta_{\text{gap}} \sim 15\text{AU}$  and  $(\Sigma_0 - \Sigma)/\Sigma_0 \sim 0.23$ , respectively. This is too shallow and too wide compared with that predicted by theory. However, the observations are limited to an angular resolution of  $\sim 15\text{AU}$ , and the depth and width could be deeper and narrower in reality. For instance, if we assume that the gap depth times the gap width retains the value derived from the observations, it is possible for the gap to have a width and depth of  $\Delta_{\text{gap}} \sim 6\text{AU}$  and  $(\Sigma_0 - \Sigma)/\Sigma_0 \sim 0.58$ , which is similar to the GPI result (Rapson et al. 2016). Such a gap could be opened by a super-Neptune-mass planet, depending on parameters of the disk, such as the turbulent viscosity (Kanagawa et al. 2015a,b, 2016). If the gap in the larger dust grains is deeper than that in the gas, the planet could be lighter than super-Neptune mass. We note that a planet of even a few Earth masses, although it cannot open a gap in the gas, can open a gap in the dust distribution if a certain amount of pebble-sized particles, whose motion is not perfectly coupled to that of gas, are scattered by the planet and/or the spiral density waves excited by the planet (Paardekooper & Mellema 2006; Muto & Inutsuka 2009).

Another possible mechanism to form a gap and an associated ring in dust continuum emission is the microscopic process of sintering of CO ice on dust aggregates (Okuzumi et al. 2016; Sirono 2011). The gaps and rings observed in the younger and more luminous HL Tau system could be explained by the sintering of various molecular ices in the disk at their distinct snow line locations (Okuzumi et al. 2016). Although our observations indicate that the CO depleted region is located down to  $\sim 10\text{AU}$  in the TW Hya system, model calculations of the temperature in the disk suggest the CO snow line is located at  $\sim 30\text{AU}$ . Sintering is a process that renders an aggregate less sticky (Sirono 2011). Just outside the CO snow line where sintering occurs, large aggregates become easily destroyed into small fragments by collisions and their radial drift motion by the above-mentioned mechanism slows down. Thus dust grains are stuck just outside the CO snow line, and a bright ring and a dark lane inside the ring is formed in the dust continuum emission. If another sintering region is formed inside the dark lane by, for example,  $\text{CH}_4$  sintering, the region between the bright CO and  $\text{CH}_4$  sintering regions would look like a gap. According to model calculations (Okuzumi et al. 2016), the  $\text{CH}_4$  sintering region is located at  $\sim 10\text{AU}$  in the TW Hya disk.

### 4.2. CO Gas Depletion inside the CO Snow Line

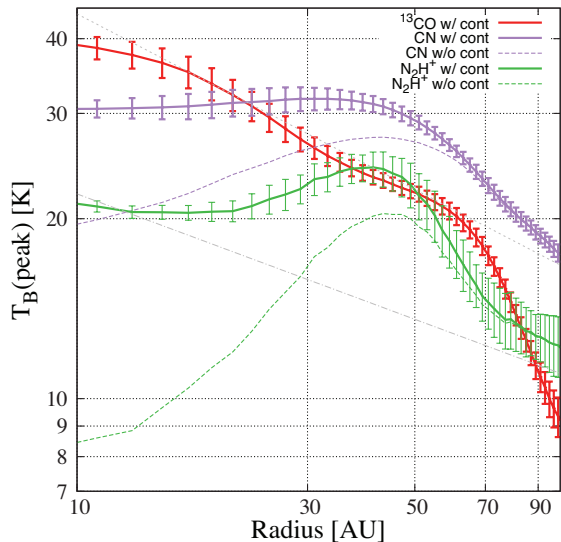


FIG. 5.— Radial distributions of the observed brightness temperature at the peak of  $^{13}\text{CO } J = 3 - 2$  (red) and  $\text{N}_2\text{H}^+ J = 4 - 3$  (green) lines. The dust temperature at the midplane (dot-dashed gray line) and the brightness temperature of  $\text{CN } N = 3 - 2$  (purple) line are also plotted for comparison. Dashed lines show the data subtracted by the dust continuum emission for  $\text{N}_2\text{H}^+$  and  $\text{CN}$ . All data are smoothed to a beam size of  $0.45 \times 0.45$ .

From the CO line observations, we find a very low column density of CO compared with dust throughout the disk down to a radius of about 10 AU. This CO depletion could indicate a general absence of  $\text{H}_2$  gas compared with dust. However, the Herschel HD observations (Bergin et al. 2013) indicates that it is more likely that it is due to CO freeze-out on grains with the possibility that subsequent grain surface reactions form larger molecules even inside the CO snow line (Favre et al. 2013; Williams & Best 2014). The CO column density derived from our observations,  $N_{\text{CO}} \sim 10^{18} \text{ cm}^{-2}$ , can be explained by detailed model calculations using a chemical network which includes freeze-out of molecules on grains and grain-surface reactions (Aikawa et al. 2015). The model calculations show the CO depletion will proceed inside the CO snow line due to the sink effect: conversion of CO to less volatile species on grain surface. In the case of TW Hya, it could occur on a timescale shorter than the disk lifetime, depending on the amount of small grains. See Aikawa et al. (2015) for more detailed discussions including the effect on other species. The CO depletion spread over the disk is inconsistent with the prediction by the previous ALMA  $\text{N}_2\text{H}^+$  observations that depletion would be localized beyond the CO snow line (Qi et al. 2013). This could be because the  $\text{N}_2\text{H}^+$  line emission traces the disk surface and not the CO depleted region.

Fig. 5 shows the brightness temperature at the peak of the  $^{13}\text{CO } J = 3 - 2$  line obtained by our observations and the  $\text{N}_2\text{H}^+ J = 4 - 3$  line at 372.672 GHz

obtained by the ALMA archived data (2011.0.00340.S). Since the  $^{13}\text{CO}$  line is optically thick, the brightness temperature at the peak of the line emission represents the gas temperature of the line emitting region. If LTE is applicable, the  $\text{N}_2\text{H}^+$  brightness temperature is higher than the gas temperature of the  $^{13}\text{CO}$  line emitting region at the disk radius of  $\sim 40$  AU, and higher than the dust temperature near the midplane down to  $\sim 15$  AU (Fig. 5). If the  $\text{N}_2\text{H}^+$  line is optically thin, the gas temperature of the line emitting region is higher than the brightness temperature. Therefore, the  $\text{N}_2\text{H}^+$  line should come from the surface layer of the disk. Model calculations also predict that  $\text{N}_2\text{H}^+$  exists in the disk surface for the model with (sub)micron-sized grains, similar to radical species abundant in the disk surface, such as CN and  $\text{C}_2\text{H}$  (e.g., Walsh et al. 2010; Aikawa et al. 2015). Our results (Fig. 5) and the SMA observations of  $\text{C}_2\text{H}$  (Kastner et al. 2015) show that the radial intensity profiles of these species are similar. They have peaks around the disk radius of 40 AU beyond which the dust surface density drops. The result suggests that in order to trace the CO depleted region, the  $\text{C}^{18}\text{O}$  line may be more robust than the  $\text{N}_2\text{H}^+$  line.

In the CO depleted region complex organic molecules would be produced via grain surface reactions since hydrogen attachment to CO is thought to produce methanol and more complex species (e.g., Watanabe & Kouchi 2008; Walsh et al. 2014a). Methyl cyanide, which has recently been detected from a protoplanetary disk for the first time by ALMA (Öberg et al. 2015), could be formed through such grain surface reactions.

We would like to thank the referee for his/her comments which improved our paper. We are also grateful to Sean Andrews and Joel Kastner for their fruitful comments. This paper makes use of the following ALMA data: ADS/JAO.ALMA#2013.1.01397.S and ADS/JAO.ALMA#2011.0.00340.S. ALMA is a partnership of ESO (representing its member states), NSF (USA) and NINS (Japan), together with NRC (Canada), NSC and ASIAA (Taiwan) and KASI (Republic of Korea), in cooperation with the Republic of Chile. The Joint ALMA Observatory is operated by ESO, AUI/NRAO and NAOJ. This work is partially supported by Grants-in-Aid for Scientific Research, 23103005, 25108004, 25400229 and 15H03646. T.T. was supported by JSPS KAKENHI grant No. 23103004. C.W. is supported by the Netherlands Organisation for Scientific Research (program number 639.041.335). Astrophysics at QUB is supported by a grant from the STFC.

*Facility:* ALMA.

## REFERENCES

- Aikawa, Y., Furuya, K., Nomura, H., & Qi, C. 2015, *ApJ*, 807, 120  
 Akiyama, E., Muto, T., Kusakabe, N. et al. 2015, *ApJ*, 802, L17  
 ALMA Partnership, Brogan, C. L., Pérez, L. M. et al. 2015, *ApJ*, 808, L3  
 Andrews, S. M., Wilner, D. J., Hughes, A. M. et al. 2012, *ApJ*, 744, 162  
 Bergin, E. A., Cleeves, L. I., Gorti, U. et al. 2013, *Nature*, 493, 644  
 Favre, C., Cleeves, L. I., Bergin, E. A., Qi, C., & Blake, G. A. 2013, *ApJ*, 776, L38  
 Fung, J., Shi, J.-M., & Chiang, E. 2014, *ApJ*, 782, 88  
 Goldreich, P., & Tremaine, S. 1980, *ApJ*, 241, 425

- Hernández, J., Hartmann, L., Megeath, T., et al. 2007, *ApJ*, 662, 1067
- Hogerheijde, M. R., Bekkers, D., Pinilla, P., Salinas, V. N., Kama, M., Andrews, S. M., Qi, C., & Wilner, D. J. 2016, *A&A*, 589, A99
- Ida, S., Lin, D. N. C., & Nagasawa, M. 2013, *ApJ*, 775, 42
- Kanagawa, K. D., Muto, T., Tanaka, H., Tanigawa, T., Takeuchi, T., Tsukagoshi, T., & Momose, M. 2015a, *ApJ*, 806, L15
- . 2016, *PASJ*, submitted
- Kanagawa, K. D., Tanaka, H., Muto, T., Tanigawa, T., & Takeuchi, T. 2015b, *MNRAS*, 448, 994
- Kastner, J. H., Qi, C., Gorti, U., Hily-Blant, P., Oberg, K., Forveille, T., Andrews, S., & Wilner, D. 2015, *ApJ*, 806, 75
- Kikuchi, A., Higuchi, A., & Ida, S. 2014, *ApJ*, 797, 1
- Kley, W., & Nelson, R. P. 2012, *ARA&A*, 50, 211
- Kuzuhara, M., Tamura, M., Kudo, T., et al. 2013, *ApJ*, 774, 11
- Lin, D. N. C., & Papaloizou, J. 1979, *MNRAS*, 186, 799
- Miotello, A., Bruderer, S., & van Dishoeck, E. F. 2014, *A&A*, 572, A96
- Muto, T., & Inutsuka, S.-i. 2009, *ApJ*, 695, 1132
- Muto, T., Grady, C. A., Hashimoto, J., et al. 2012, *ApJ*, 748, L22
- Öberg, K. I., Guzmán, V. V., Furuya, K., Qi, C., Aikawa, Y., Andrews, S. M., Loomis, R., & Wilner, D. J. 2015, *Nature*, 520, 198
- Okuzumi, S., Momose, M., Sirono, S.-i., Kobayashi, H., & Tanaka, H. 2016, *ApJ*, in press (astro-ph/1510.03556)
- Paardekooper, S.-J., & Mellema, G. 2006, *A&A*, 453, 1129
- Qi, C., D'Alessio, P., Öberg, K. I., Wilner, D. J., Hughes, A. M., Andrews, S. M., & Ayala, S. 2011, *ApJ*, 740, 84
- Qi, C., Wilner, D. J., Aikawa, Y., Blake, G. A., & Hogerheijde, M. R. 2008, *ApJ*, 681, 1396
- Qi, C., Öberg, K. I., Wilner, D. J., et al. 2013, *Science*, 341, 630
- Rapson, V. A., Kastner, J. H., Millar-Blanchaer, M. A., & Dong, R. 2015, *ApJ*, 815, L26
- Rybicki, G. B., & Lightman, A. P. 1979, *Radiative processes in astrophysics* (New York: Wiley)
- Sirono, S.-i. 2011, *ApJ*, 735, 131
- Takeuchi, T., Clarke, C. J., & Lin, D. N. C. 2005, *ApJ*, 627, 286
- Thalmann, C., Carson, J., Janson, M., et al. 2009, *ApJ*, 707, L123
- Turner, B. E. 1991, *ApJS*, 76, 617
- Walsh, C., Millar, T. J., & Nomura, H. 2010, *ApJ*, 722, 1607
- Walsh, C., Millar, T. J., Nomura, H., Herbst, E., Widicus Weaver, S., Aikawa, Y., Laas, J. C., & Vasyunin, A. I. 2014a, *A&A*, 563, A33
- Walsh, C., Juhász, A., Pinilla, P., et al. 2014b, *ApJ*, 791, L6
- Watanabe, N., & Kouchi, A. 2008, *Progress In Surface Science*, 83, 439
- Williams, J. P., & Best, W. M. J. 2014, *ApJ*, 788, 59
- Zhang, K., Bergin, E. A., Blake, G. A., Cleeves, L. I., Hogerheijde, M., Salinas, V., & Schwarz, K. R. 2016, *ApJ*, 818, L16